International Symposium
On Turbulence and Shear Flow
Phenomena (TSFP-9)
June 30 - July 3, 2015 *Melbourne, Australia*

TURBULENT DISPERSION FROM A POINT SOURCE AT DIFFERENT RELEASE LOCATIONS WITHIN AN URBAN CANOPY MODEL

Mohammad Saeedi
Department of Mechanical Engineering
University of Manitoba
Winnipeg, MB, R3T 5V6, Canada
umsaeedi@myumanitoba.ca

Bing-Chen Wang*
Department of Mechanical Engineering
University of Manitoba
Winnipeg, MB, R3T 5V6, Canada
BingChen.Wang@umanitoba.ca

ABSTRACT

In this research, wall-modeled LES has been performed to investigate turbulent flow and dispersion of concentration from a continuous ground-level point source within a modeled urban environment. Two different release locations (behind and between obstacles) of the concentration have been tested. Owing to the exceptionally high inlet turbulence level, an inflow boundary condition based on generation of grid turbulence is proposed to mimic the approaching turbulent boundary layer in a water channel. Turbulent coherent flow structures and budget balance of resolved kinetic energy are thoroughly studied. The first- and second-order statistics of the velocity and concentration fields obtained from the simulations are validated against the water-channel measurement data.

Introduction

Turbulent flow and dispersion over a group of bluff bodies are frequently encountered in engineering applications. Over the past two decades, turbulent flow and dispersion in urban environments has become an important problem due to the increasingly growing need to understand and predict accidental and deliberate release of toxic pollutants in urban complexes. Recent important studies of urban flow include Basel UrBan Boundary Layer Experiment (BUBBLE) which measured the wind flow through and above a homogeneous urban area by Rotach *et al.* (2004), Mock Urban Setting Trial (MUST) conducted at US Army Dugway Proving Ground which studied plume dispersing through an array of building-size obstacles by Yee & Biltoft (2004), and the study of Brown *et al.* (2001) who performed high resolution measurements of turbulence statistics along the centerline plane of an array of obstacles immersed in a simulated atmospheric boundary-layer. A series of high-quality water channel experiments were conducted by Yee *et al.* (2006) in which turbulent flow over a matrix of wall-mounted obstacles along with continuous release of contaminant at different positions were investigated.

Hanna *et al.* (2002) performed large-eddy simulation (LES) over different arrays of wall-mounted obstacles immersed in a fully-developed boundary-layer. They compared regular and staggered arrays of obstacles and showed that the flow acceleration in canyon regions was higher in the regular array than that in the staggered array. Coceal *et al.* (2006) performed DNS over staggered and aligned wall-mounted cubes at a relatively low Reynolds number. They revealed the importance of the layout of obstacles and highlighted the need for considering three-dimensionality of the flow in urban-like environments. Cheng *et al.* (2003) compared the effectiveness of LES and Reynolds-averaged Navier-Stokes (RANS) approaches in simulating the turbulent flow over a matrix of cubes at a relatively low Reynolds number. They observed a better performance of LES in terms of the prediction of Reynolds stresses and spanwise mean velocity. Wang *et al.* (2009) used a non-linear k-ε model for simulating instantaneous release of contaminant from a ground-level point source. They proposed a so-called dissipation length-scale model required for closure of the concentration variance equation. In their follow-up study of length scale models for the concentration variance dissipation rate, Wang *et al.* (2010) numerically investigated the turbulent dispersion of a passive scalar released from a continuous ground-level point-source using the RANS approach and were able to well reproduce the experimental results of the mean and second-order concentration fields. Kim & Baik (2004) used a RANS approach to investigate the effect of wind direction on the spatial distribution of a passive scalar in an idealized urban area. They showed that when the flow direction was perpendicular to the windward face of a modeled building obstacle, a high concentration zone was formed on its leeward side, however, the mean concentration level was diagonally symmetric when the incident angle was 45°.

In this research, we perform wall-modeled LES of plume dispersion released from a point source located in the canyon region of a matrix of 3-D wall-mounted obstacles. The objective of this research is to investigate highly-disturbed flow using well-designed inlet conditions, trans-

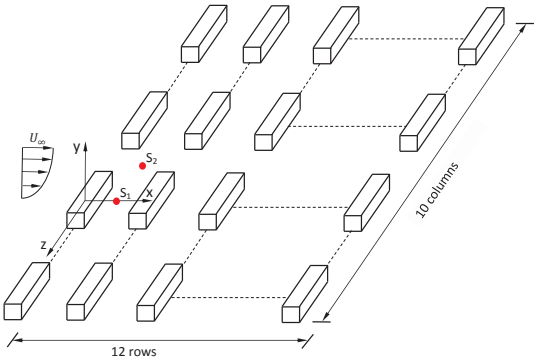

Figure 1. Schematic of the matrix of 10×12 wall-mounted obstacles.

port mechanisms of the kinetic and scalar energy, and interaction of the concentration field with the dynamically evolving flow structures. LES has been conducted using an in-house computer code on public-domain computer clusters of the Western Canada Research Grid (WestGrid).

Test case

The simulation is to reproduce one of the water-channel experiments of Yee *et al.* (2006) on turbulent flow and dispersion in a modeled urban environment. In their experiment, a regular array of 10×12 wall-mounted rectangular obstacles with side-length of $d = 11.8$ mm, height of $h = 12.4$ mm and width of $l = 59.4$ mm were immersed in an emulated neutrally stratified atmospheric boundary layer. The Reynolds number based on the obstacle height and the free-stream velocity ($U_\infty = 0.38m/s$) was 4,700. A passive tracer was released from a ground-level point source, and two sources locations (S_1 and S_2) were tested. Figure 1 shows the schematic of the matrix of obstacles and two locations of the point source. Given the fact that the flow conditions are symmetric in the spanwise directions, a regular matrix of 5×12 obstacles have been considered in the current simulation. In total, $640 \times 40 \times 352$ grid points are used to discretize the domain in the streamwise, vertical and spanwise directions respectively.

Algorithm and SGS models

For LES of turbulent dispersion in the context of an incompressible boundary layer flow, the governing equations take the following form

$$\frac{\partial \bar{u}_i}{\partial x_i} = 0, \tag{1}$$

$$\frac{\partial \bar{u}_i}{\partial t} + \frac{\partial \bar{u}_i \bar{u}_j}{\partial x_j} = -\frac{1}{\rho}\frac{\partial \bar{p}}{\partial x_i} + \nu \frac{\partial^2 \bar{u}_i}{\partial x_j \partial x_j} - \frac{\partial \tau_{ij}}{\partial x_j}, \tag{2}$$

$$\frac{\partial \bar{c}}{\partial t} + \frac{\partial}{\partial x_j}(\bar{u}_j \bar{c}) = \alpha \frac{\partial^2 \bar{c}}{\partial x_j \partial x_j} - \frac{\partial h_j}{\partial x_j}, \tag{3}$$

where $\bar{u}_i$, $\bar{p}$ and $\bar{c}$ represent the filtered velocity, pressure and scalar fields respectively, ν is the kinematic viscosity of the fluid, α is the molecular diffusivity of the scalar and τ_{ij} and h_j are the so-called subgrid-scale (SGS) stress tensor and SGS scalar flux vector, respectively. The SGS stress and scalar flux appear in the governing system of equations as a result of the filtering process and are defined as $\tau_{ij} = \overline{u_i u_j} - \bar{u}_i \bar{u}_j$ and $h_j = \overline{u_j c} - \bar{u}_j \bar{c}$, respectively. In order to close the above system of governing equations, the SGS stress tensor and SGS scalar flux vector need to be modeled. The SGS stress model used for closing the filtered governing equations is the dynamic non-linear model (DNM) proposed by Wang & Bergstrom (2005), which expresses the SGS stress tensor as

$$\tau^*_{ij} = -C_S \beta_{ij} - C_W \gamma_{ij} - C_N \eta_{ij}, \tag{4}$$

where the base tensors are defined as $\beta_{ij} \stackrel{\text{def}}{=} 2\bar{\Delta}^2 |\bar{S}| \bar{S}_{ij}$, $\gamma_{ij} \stackrel{\text{def}}{=} 4\bar{\Delta}^2 (\bar{S}_{ik}\bar{\Omega}_{kj} + \bar{S}_{jk}\bar{\Omega}_{ki})$ and $\eta_{ij} \stackrel{\text{def}}{=} 4\bar{\Delta}^2 (\bar{S}_{ik}\bar{S}_{kj} - \bar{S}_{mn}\bar{S}_{nm}\delta_{ij}/3)$. Here, $\bar{S}_{ij} \stackrel{\text{def}}{=} (\partial \bar{u}_i/\partial x_j + \partial \bar{u}_j/\partial x_i)/2$ is the resolved strain rate tensor, $\bar{\Omega}_{ij} \stackrel{\text{def}}{=} (\partial \bar{u}_i/\partial x_j - \partial \bar{u}_j/\partial x_i)/2$ is the resolved rotation rate tensor, $|\bar{S}| = \sqrt{2\bar{S}_{ij}\bar{S}_{ij}}$ is the norm of $\bar{S}_{ij}$, δ_{ij} is the Kronecker delta, and an asterisk superscript denotes the trace-free form of a tensor. Following the least squares procedure, the local dynamic model coefficients can be obtained, viz.

$$\begin{bmatrix} M_{ij}M_{ij} & M_{ij}W_{ij} & M_{ij}N_{ij} \\ W_{ij}M_{ij} & W_{ij}W_{ij} & W_{ij}N_{ij} \\ N_{ij}M_{ij} & N_{ij}W_{ij} & N_{ij}N_{ij} \end{bmatrix} \cdot \begin{bmatrix} C_S \\ C_W \\ C_N \end{bmatrix} = - \begin{bmatrix} \mathscr{L}^*_{ij}M_{ij} \\ \mathscr{L}^*_{ij}W_{ij} \\ \mathscr{L}^*_{ij}N_{ij} \end{bmatrix}. \tag{5}$$

where $\mathscr{L}_{ij} \stackrel{\text{def}}{=} \widetilde{\bar{u}_i \bar{u}_j} - \tilde{\bar{u}}_i \tilde{\bar{u}}_j$ is the resolved Leonard type stress; $M_{ij} \stackrel{\text{def}}{=} \alpha_{ij} - \tilde{\beta}_{ij}$, $W_{ij} \stackrel{\text{def}}{=} \lambda_{ij} - \tilde{\gamma}_{ij}$ and $N_{ij} \stackrel{\text{def}}{=} \zeta_{ij} - \tilde{\eta}_{ij}$ are differential tensors; and $\alpha_{ij} \stackrel{\text{def}}{=} 2\tilde{\bar{\Delta}}^2 |\tilde{\bar{S}}| \tilde{\bar{S}}_{ij}$, $\lambda_{ij} \stackrel{\text{def}}{=} 4\tilde{\bar{\Delta}}^2 (\tilde{\bar{S}}_{ik}\tilde{\bar{\Omega}}_{kj} + \tilde{\bar{S}}_{jk}\tilde{\bar{\Omega}}_{ki})$ and $\zeta_{ij} \stackrel{\text{def}}{=} 4\tilde{\bar{\Delta}}^2 (\tilde{\bar{S}}_{ik}\tilde{\bar{S}}_{kj} - \tilde{\bar{S}}_{mn}\tilde{\bar{S}}_{nm}\delta_{ij}/3)$ are base tensors at the test-grid level.

The eddy diffusivity model (EDM) proposed by Moin *et al.* (1991) has been used for determining the SGS scalar flux which expresses the SGS scalar flux vector as

$$h_j = -C_\theta \bar{\Delta}^2 |\bar{S}| \frac{\partial \bar{c}}{\partial x_j}, \tag{6}$$

where $\frac{\partial \bar{c}}{\partial x_j}$ is the mean concentration gradient. The dynamic model coefficient can be obtained as

$$C_\theta = -\frac{\mathscr{L}_j M_j}{M_i M_i}, \tag{7}$$

where $\mathscr{L}_j \stackrel{\text{def}}{=} \widetilde{\bar{u}_j \bar{c}} - \tilde{\bar{u}}_j \tilde{\bar{c}}$ is the resolved scalar flux vector which can be directly computed from the filtered velocity and scalar fields and $M_j \stackrel{\text{def}}{=} a_j - \tilde{b}_j$ is a differential vector. Here, b_j and a_j are two base vectors at the grid-level and test-grid-level, respectively, defined as $b_j \stackrel{\text{def}}{=} \bar{\Delta}^2 |\bar{S}| \frac{\partial \bar{c}}{\partial x_j}$ and $a_j \stackrel{\text{def}}{=} \tilde{\bar{\Delta}}^2 |\tilde{\bar{S}}| \frac{\partial \tilde{\bar{c}}}{\partial x_j}$.

LES has been conducted using an in-house code developed using FORTRAN 90/95 programming languages and parallelized using message passing interface (MPI) libraries. The governing equations have been discretized using a second-order fully conservative finite difference discretization scheme based on a staggered grid arrangement. A fully implicit four-level fractional step method coupled

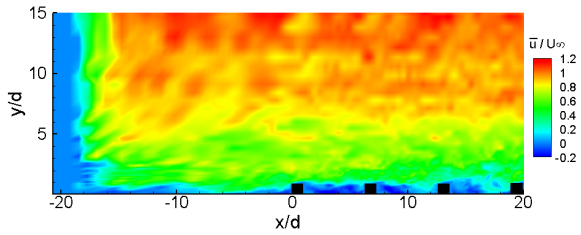

(a) approaching region

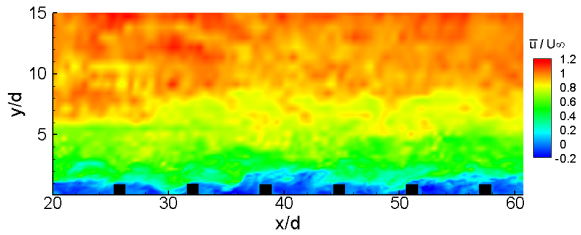

(b) obstacle region

Figure 2. Contours of the resolved instantaneous streamwise velocity in the central x-y plane (located at $z/d = 0$).

with a second-order Crank-Nicolson scheme has been used to advance the velocity field over a single time step. The Poisson equation for pressure correction is solved using a four-level V-cycle multigrid method. A second-order total variation diminishing (TVD) scheme is used for discretizing the convection term of the scalar transport equation.

Boundary conditions

In order to evaluate the wall shear stress, the stress-balance wall model with the pressure gradient term of Wang & Moin (2002) has been applied to solid surfaces. As such, the wall parallel component of the wall shear stress (τ_{wi}) is obtained as

$$\tau_{wi} = \mu \frac{\partial \bar{u}_i}{\partial x_n}\Big|_{x_n=0} = \frac{\rho}{\int_0^\delta \frac{dx_n}{\nu+\nu_t}} \left(\bar{u}_{\delta_i} - \frac{1}{\rho} \frac{\partial \bar{p}}{\partial x_i} \int_0^\delta \frac{x_n dx_n}{\nu+\nu_t} \right), \quad (8)$$

where δ is the height of the first grid point off the wall, n is the wall normal direction, $\bar{u}_{\delta_i}$ is the wall-parallel velocity component at height δ taken from outer LES solution and ν_t is the turbulent eddy viscosity which can be obtained from the mixing length as

$$\nu_t/\nu = \kappa \delta^+ D^2, \quad (9)$$

where κ is the Kármán constant, δ^+ is the non-dimensional normal distance from the wall, $D = 1 - \exp(-\delta^+/A^+)$ is the damping function and $A^+ = 19$ (recommended by Wang & Moin (2002)) is the van Driest constant.

One of the main challenges for conducting this simulation is to prescribe proper inlet boundary conditions to realistically regenerate the exceptionally high approaching turbulence level (which is at least 10%). In this research, after testing several inlet conditions, the inlet turbulence is generated using a solid grid mounted at the inlet boundary. Figures 2a and 2b show the instantaneous streamwise velocity contours in the x-y plane located at $z/d = 0$ in the approaching and obstacle regions, respectively. As is evident in Fig. 2a, turbulence is triggered right behind the grid

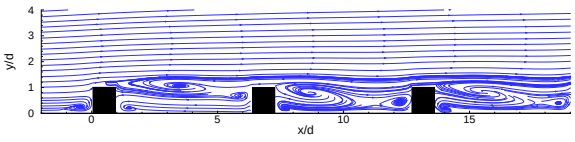

(a) rows 1-3

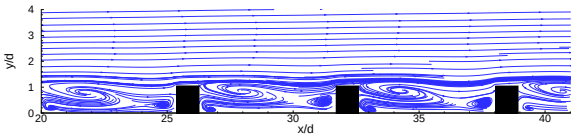

(b) rows 4-7

Figure 3. Time-averaged streamlines around obstacles in different rows, demonstrated in the central x-y plane (at $z/d = 0$).

location at $x/d \approx -22$ and as the distance from the inlet increases, the turbulent patches quickly become uniform, reaching a stable sustainable level in the obstacle region. Neumann boundary condition is applied to the outlet boundary and slip condition is considered for the upper boundary.

Result analysis

Flow field

The qualitative characteristics of the highly-disturbed flow within and above the obstacles have been vividly demonstrated using the contours of the resolved streamwise instantaneous velocity in Fig. 2. In order to have a better understanding of the vortical structures in the obstacle region, Fig. 3 shows the time-averaged streamlines in the central x-y plane around the first seven rows of obstacles. As shown in Fig. 3a, a large vortex is observed in the stagnant region (impinging zone) in front of the first row of obstacles. This is the signature of the horseshoe vortex formed in front of the first row of obstacles, which will be thoroughly discussed in the next paragraph. Also, a small recirculation region has been formed only above the rooftop of the first obstacle which is due to the strike of the flow at the sharp front edge of the obstacle. At the rooftop of the first obstacle, a strong shear layer and large mean velocity gradient form, which further trigger flow instability and induce boundary layer separation. It is also clearly observed in Figs. 3a and 3b that the vortical structures (in terms of the location and size of recirculating vortices between the obstacles) in the canyon regions gradually evolve towards a self-similar state as the distance from the first row increases. The size and pattern of recirculating vortices between two adjacent obstacles become increasingly similar after the fifth row.

In order to analyze the structure of the horseshoe vortex formed around the first row of obstacles, a top view of contours of time-averaged pressure coefficient (defined as $C_p = (\bar{p} - \bar{p}_\infty)/q_\infty$, where $\bar{p}_\infty$ is the resolved free-stream pressure and $q_\infty = \frac{1}{2}\rho U_\infty^2$ is the free-stream dynamic pressure) superimposed with time-averaged streamlines is shown in the central column (for $-4 < x/d < 6$ and $-4 < z/d < 4$) at elevation $y/d = 0.2$ in Fig. 4. As is evident in Fig. 4, a stagnant zone is formed in the immediate adjacency of the windward face of the first-row obstacles due to the impingement of the flow onto the obstacle. The high stagnation pressure then causes the reverse flow towards the saddle point

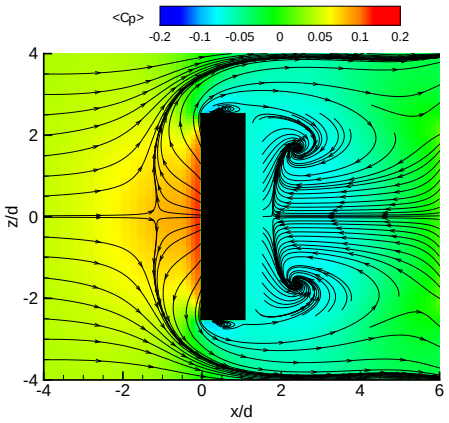

Figure 4. Horseshoe vortex in front of the first-row obstacle in the central column, visualized using time-averaged pressure coefficient and streamlines in the x-z plane at elevation $y/d = 0.2$.

of the horseshoe vortex. It shows intuitively in Fig. 4 that the horseshoe streamline pattern in the front of the obstacle is a result of this reverse flow and the approaching flow from the upstream. Also, it is clear that due to the acceleration of the flow on both sides of the obstacle, the pressure value drops significantly in side regions of the obstacle. In comparison with the high pressure level in front of the windward face of the obstacle, the pressure level behind the obstacle is much lower. This pressure difference between the front and the rear of the obstacle is the exact cause of the form drag in building aerodynamics and wind engineering. Also, the low pressure zone behind the obstacle creates a strong suction effect and causes the flow coming from side regions of the obstacle to circulate towards the focal points of the horseshoe vortex.

In order to validate the simulated velocity field, first- and second-order turbulence statistics obtained from the simulation have been compared against the available experimental data. For this purpose, two different locations before and behind the central obstacle of the matrix of obstacles (the obstacle in the middle column and the sixth row) have been selected for comparison. More specifically, vertical profiles have been extracted from positions $x/d = 30.25$ and $x/d = 33.9$ at $z/d = 0$ which are approximately $1.5d$ before and behind the obstacle. Details on the description of measurement locations can be found in Wang *et al.* (2009). Figures 5a and 5b compare the profiles of the predicted and measured time-averaged streamwise velocity at the selected locations. As is evident in both figures, very good agreement between the predicted results and experimental data is observed. The strong shear layer close to the ground and the reverse flow (negative velocity) are in consistence with the qualitative results shown in Fig. 3.

In Figs. 6a and 6b, the profiles of the streamwise RMS velocity (or the streamwise turbulence intensity) at the same locations as for Fig. 5 have been presented. As shown in Figs. 6a and 6b, at both locations, the maximum RMS velocity occurs at $y/d \approx 1$ which is due to the intense turbulence activities associated with the strong shear layer issued by the obstacle top surface. The shape of the profiles and the locations of the maximum RMS velocities have been well predicted by the simulation. However, the magnitude of the RMS velocity on regions above the obstacle height ($y/d > 1$) has been slightly under-predicted. This is due to

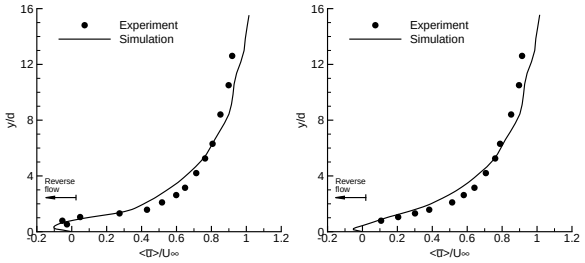

(a) before the mid obstacle (b) behind the mid obstacle

Figure 5. Vertical profiles of the mean streamwise velocity before and behind the mid obstacle (for $z/d = 0$).

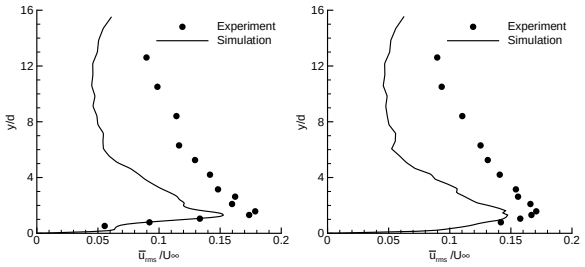

(a) before the mid obstacle (b) behind the mid obstacle

Figure 6. Vertical profiles of the streamwise RMS velocity before and behind the mid obstacle (for $z/d = 0$).

the exceptionally high turbulence level in this region discussed in the boundary condition subsection.

Figures 7a and 7b show the cross-stream budget balance of the resolved kinetic energy (KE) of the flow (defined $k_r \stackrel{\text{def}}{=} \frac{1}{2}\overline{u}_i\overline{u}_i$) in the self-similarity region at mid-point between rows 6 and 7 ($x/d = 35.3$) at two different elevations for $y/d = 0.75$ and 1.5. As shown in Fig. 7a, at elevation $y/d = 0.75$, the advection ($\langle \overline{u}_j \frac{\partial k_r}{\partial x_j} \rangle$), pressure diffusion ($-\frac{1}{\rho}\langle \overline{u}_j \frac{\partial \overline{p}}{\partial x_j} \rangle$) and SGS dissipation rate ($\langle \tau^*_{ij}\overline{S}_{ij} \rangle$) are the dominant terms in the transport equation of k_r, and furthermore, the advection term is primarily balanced by the pressure diffusion and SGS dissipation terms. The peak values of advection and pressure diffusion occur at $z/d \approx \pm 2.5$, directly downstream of the two sides of the obstacle. At these locations, the flow in the canyons strikes the two vertical side edges of the obstacle, forming a strong shear layer on each side which further triggers the flow instability and entrains the recirculating region immediately behind the obstacle. As a consequence of the enhanced turbulence level due to the pressure difference between side and rear regions of the obstacle and strong shear layers formed on both sides of the obstacle, the magnitudes of the pressure diffusion and advection terms peak around $z/d \approx \pm 2.5$. Also, there is a local minima in the central region behind the obstacle which reflects the low turbulence level inside the recirculation bubble behind the obstacle. The overall influence of viscous diffusion ($2\nu\langle \frac{\partial \overline{S}_{ij}\overline{u}_i}{\partial x_j} \rangle$) and viscous dissipation rate ($-2\nu\langle \overline{S}_{ij}\overline{S}_{ij} \rangle$) are not significant in comparison with other terms, because this flow (with exceptionally high free-stream turbulence level and strong disturbances from obstacles) is dominated by inertial forces rather than viscous forces. As shown in Fig. 7a, the level of SGS diffusion is much smaller than that of SGS dissipation. This is because

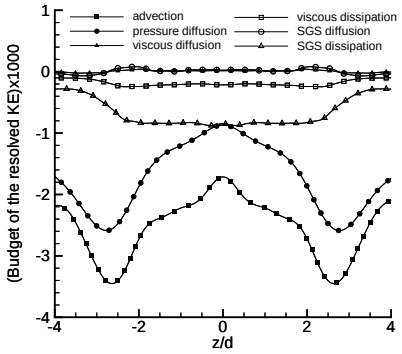

(a) $y/d = 0.75$

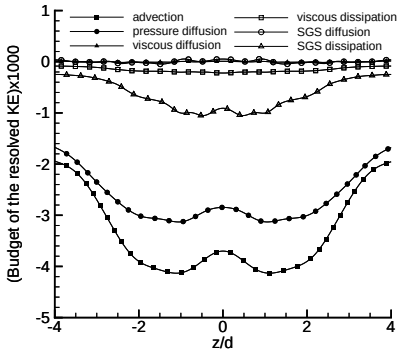

(b) $y/d = 1.5$

Figure 7. Budget of the time-averaged resolved kinetic energy (k_r) at $x/d = 35.3$ within $-4 < z/d < 4$, at two different elevations. All the quantities shown in the figures have been non-dimensionalized using U_∞^3/d.

the SGS dissipation term $\langle \tau_{ij}^* \bar{S}_{ij} \rangle$ represents KE transfer between the large resolved and small subgrid scales, or interaction of eddy motions of these two different scales. The SGS dissipation rate reflects a major feature of SGS dynamics, as it represents a key physical quantity that determines the cascade of energy in LES. In contrast, the SGS diffusion represents diffusion (or, re-distribution) of KE due to SGS shear stresses (which are much smaller than resolved turbulent shear stresses), and its value is expected to be smaller than that of the SGS dissipation rate.

Figure 7b shows the cross-stream budget balance of the resolved kinetic energy k_r at the same streamwise location but above the canopy at $y/d = 1.5$. As is evident in Fig. 7b, the advection term is primarily balanced by the pressure diffusion term. By comparing Figs. 7b and 7a, it is evident that the local maxima of the advection and pressure diffusion have been shifted toward the central region downstream of the obstacle. This shows that above the canopy, the impact of the separated shear layers from the obstacle sides have been much reduced and at $y/d = 1.5$, the flow is significantly influenced by the separated boundary layer from the obstacle rooftop.

Concentration field

In order to qualitatively demonstrate the evolution of the concentration field within the flow domain and compare the effects of different release locations on the concentration field, Figs. 8a and 8b present the instantaneous concentration fields in the x-z plane (located at $y/d = 0.5$) for cases S_1 and S_2, respectively. As is evident in Fig. 8a, when the

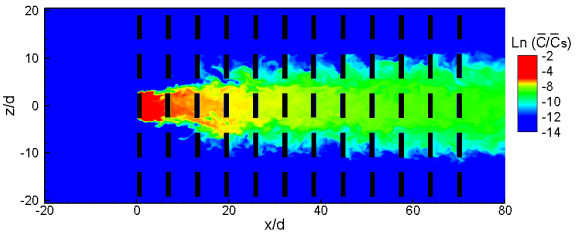

(a) case S_1

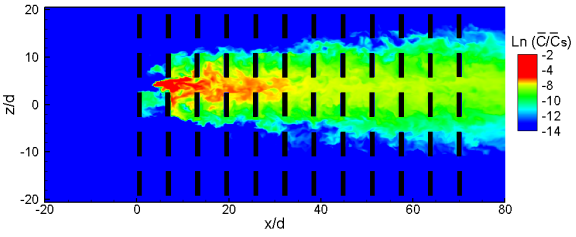

(b) case S_2

Figure 8. Contours of the instantaneous resolved concentration field ($\bar{c}$) in the x-z plane located at $z/d = 0.5$.

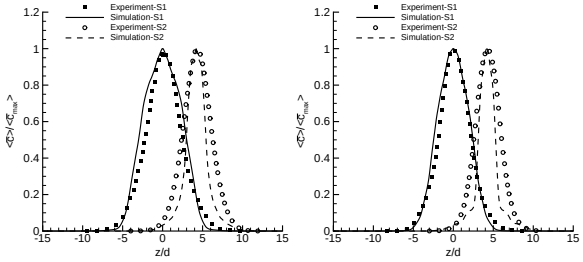

(a) under canopy (b) above canopy

Figure 9. Cross-stream profiles of the non-dimensionalized mean concentration for cases S_1 and S_2 at $x/d = 10.2$ for elevations $y/d = 0.75$ and 1.5.

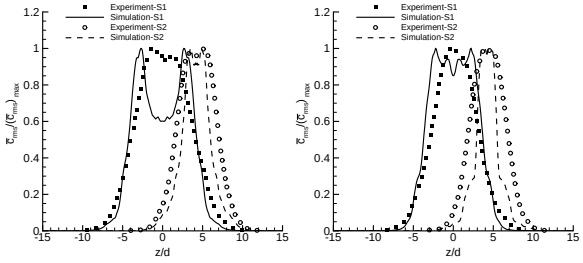

(a) under canopy (b) above canopy

Figure 10. Cross-stream profiles of the non-dimensionalized standard deviation of the concentration for cases S_1 and S_2 at $x/d = 10.2$ for elevations $y/d = 0.75$ and 1.5.

point source is located in the central plane at $z/d = 0$, a high concentration zone is formed between the first- and second-row obstacles in the central column and then the concentration disperses downstream through the side regions of the second-row obstacle. However, as shown in Fig. 8b, when the point source is in the middle of the streamwise street, the concentration is quickly washed out by the main stream. As such, in comparison with Fig. 8a, a lower concentration level in the canyon regions is observed in Fig. 8b.

Figures 9a and 9b compare the predicted and measured cross-stream profiles of the mean concentration between the first and second rows of obstacles (at $x/d = 10.2$) below and above the canopy (at elevations $y/d = 0.75$ and 1.5), respectively. In order to make the profiles comparable, the mean concentrations have been non-dimensionalized using the local maximum value along the cross-stream lines. As is evident in Fig. 9, for both elevations below and above the canopy, the plume center is located directly downstream of the point source which is $z/d = 0$ for case S_1 and $z/d = 4.2$ for case S_2. It is observed in both Figs. 9a and 9b that the plume width for case S_1 is generally wider than that for case S_2. This is attributed to the fact that for case S_1, the point source is located upstream of the central obstacle of the second row which blocks the streamwise flow and as a consequence, the plume is diverted in the spanwise direction. In Figs. 10a and 10b, the predicted cross-stream profiles of the non-dimensionalized standard deviation of the concentration for cases S_1 and S_2 have been compared against the experimental measurement data. It is observed in that the rate of decay of the standard deviation of the concentration field have been well predicted by the simulation, however, for the case S_1, the local minima of the profiles at the center of the plume deviates slightly from the experimental data.

Conclusions

Wall-modeled LES of turbulent flow and dispersion within a modeled urban environment has been performed. One of the major challenges of the current simulation is to simulate the exceptionally high turbulence level of the approaching boundary layer. This is achieved by generation of grid turbulence at the inlet plane of the computational domain.

Due to the intense interaction of the approaching highly turbulent boundary layer with the obstacles, the flow structures exhibit complex patterns, which dynamically evolve within and above the obstacle array and have a significant impact on the transport of the momentum and scalar. The spatial flow evolution has been carefully analyzed using the time-averaged streamlines pressure contours. It is observed that after the fifth row of obstacles, the flow quickly reaches a self-similar state featuring a repeating pattern in time-averaged vortical structures in canyon regions. A horseshoe vortex is observed in front of the first-row obstacles at a low elevation as a result of the adverse pressure gradient in the windward face of the obstacles.

The budget balance of the resolved KE transport equation has been analyzed behind a typical obstacle in the self-similar region at two different elevations. It is observed that below the canopy at $y/d = 0.75$, the advection term is mainly balanced with the pressure diffusion and SGS dissipation rate. Also, the peak values of advection and pressure diffusion occur at $z/d \approx \pm 4$ due to the separated shear layers from the obstacle sides which trigger the flow instability and entrain the recirculating region immediately behind the obstacle. However, above the canopy, peaks have been shifted towards the central region behind the obstacle reflecting the effect of the strong instable shear layer formed on the rooftop and accompanied local boundary-layer separation and turbulent mixing. At this elevation, the impact of the SGS dissipation rate on the transport of k_r is still important, however, its magnitude reduces as the elevation increases from $y/d = 0.75$ to 1.5.

The dispersion field has been created by continuous release of concentration from a ground-level point source. It is observed that when the point source is located behind the obstacle, due to the larger turnover time for the plume to disperse in the spanwise direction, the concentration level is generally higher than that when the point source is positioned in the streamwise street canyon.

The predicted first- and second-order flow statistics are in good agreement with the experimental data. For the concentration field, the shape of the cross-stream profiles and rate of decay for the mean and standard deviation were well predicted by the simulations. However, the local minima of the profiles of the standard deviation of the concentration were slightly underpredicted by the simulation.

REFERENCES

Brown, M. J., Lawson, R. E., DeCroix, D. S. & Lee, R. L. 2001 Comparison of centerline velocity measurements obtained around 2D and 3D building arrays in a wind tunnel. *Tech. Rep.* LA-UR-01-4138. Los Alamos National Laboratory.

Cheng, Y., Lien, F. S., Yee, E. & Sinclair, R. 2003 A comparison of large eddy simulations with a standard $k-\varepsilon$ Reynolds-averaged Navier-Stokes model for the prediction of a fully developed turbulent flow over a matrix of cubes. *J. Wind Eng. Ind. Aero.* **91**, 1301–1328.

Coceal, O., Thomas, T. G., Castro, I. P. & Belcher, S. E. 2006 Mean flow and turbulence statistics over groups of urban-like cubical obstacles. *Boundary-Layer Meteorol.* **121**, 491–519.

Hanna, S. R., Tehranian, S., Carissimo, B., MacDonald, R. W. & Lohner, R. 2002 Comparisons of model simulations with observations of mean flow and turbulence within simple obstacle arrays. *J. Atmos. Env.* **36**, 5067–5079.

Kim, J.-J. & Baik, J.-J. 2004 A numerical study of the effects of ambient wind direction on flow and dispersion in urban street canyons using the RNG $k-\varepsilon$ turbulence model. *J. Atmos. Env.* **38**, 3039–3048.

Moin, P., Squires, K., Cabot, W. & Lee, S. 1991 A dynamic subgrid-scale model for compressible turbulence and scalar transport. *Phys. Fluids A* **3**, 2746–2757.

Rotach, M. W., Gryning, S.-E., Batchvarova, E., Christen, A. & Vogt, R. 2004 Pollutant dispersion close to an urban surface–the BUBBLE tracer experiment. *Meteorol. Atmos. Phys.* **87**, 39–56.

Wang, B.-C. & Bergstrom, D. 2005 A dynamic nonlinear subgrid-scale stress model. *Phys. Fluids* **17**, 035109, 1–15.

Wang, B.-C., Yee, E. & Lien, F.-S. 2009 Numerical study of dispersing pollutant clouds in a built-up environment. *Int. J. Heat Fluid Flow* **30**, 3–19.

Wang, B.-C., Yee, E. & Lien, F.-S. 2010 Prediction of second-order concentration statistics for dispersing plumes in obstacle arrays. *Prog. Comput. Fluid Dyn.* **10**, 252–262.

Wang, M. & Moin, P. 2002 Dynamic wall modeling for large-eddy simulation of complex turbulent flows. *Phys. Fluids* **14**, 2043–2051.

Yee, E. & Biltoft, C. A. 2004 Concentration fluctuation measurements in a plume dispersing through a regular array of obstacles. *Boundary-Layer Meteorol.* **111**, 363–415.

Yee, E., Gailis, R. M., Hill, A., Hilderman, T. & Kiel, D. 2006 Comparison of wind-tunnel and water-channel simulations of plume dispersion through a large array of bstacles with a scaled field experiment. *Boundary-Layer Meteorol.* **121**, 389–432.